# Phase-Engineered Synthesis of Centimeter-Scale 1T′- and 2H-Molybdenum Ditelluride Thin Films

**Jin Cheol Park,[†,‡] Seok Joon Yun,[†,§] Hyun Kim,[†,§] Ji-Hoon Park,[†] Sang Hoon Chae,[†] Sung-Jin An,[†,§] Jeong-Gyun Kim,[†,§] Soo Min Kim,[⊥] Ki Kang Kim,[*,∥] and Young Hee Lee[*,†,‡,§]**

[†]IBS Center for Integrated Nanostructure Physics, Institute for Basic Science (IBS), [‡]Department of Physics, and [§]Department of Energy ScienceSungkyunkwan University, Suwon 440-746, Republic of Korea, [⊥]Institute of Advanced Composite Materials, Korea Institute of Science and Technology (KIST), San101 Eunha-Ri, Bongdong-Eup, Wanju-Gun, Jeollabuk-Do 565-902, Republic of Korea, and [∥]Department of Energy and Materials Engineering, Dongguk University, Seoul 100-715, Republic of Korea

**ABSTRACT** We report the synthesis of centimeter-scale, uniform 1T′- and 2H-$MoTe_2$ thin films *via* the tellurization of Mo thin films. 1T′-$MoTe_2$ was initially grown and converted gradually to 2H-$MoTe_2$ over a prolonged growth time under a Te atmosphere. Maintaining excessive Te was essential for obtaining the stable stoichiometric 2H-$MoTe_2$ phase. Further annealing under a lower partial pressure of Te at the same temperature, followed by a rapid quenching, led to the reverse phase transition from 2H-$MoTe_2$ to 1T′-$MoTe_2$. The orientation of the 2H-$MoTe_2$ film was determined by the tellurization rate. Slow tellurization was the key for obtaining a highly oriented 2H-$MoTe_2$ film over the entire area, while fast tellurization led to a 2H-$MoTe_2$ film with a randomly oriented *c*-axis.

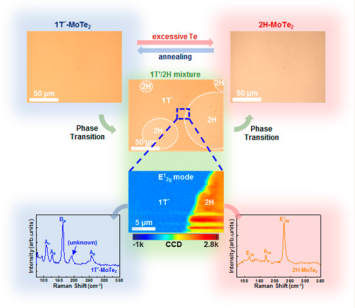


**KEYWORDS:** molybdenum ditelluride · phase transition · phase engineering · chemical vapor deposition · tellurization

Inorganic two-dimensional (2D) transition metal dichalcogenides ($MX_2$: TMDCs) consist of a transition metal (M: Mo and W, both in group VI) and chalcogenides (X: S, Se, and Te). TMDC layers are stacked layer-by-layer by van der Waals interactions.[1−3] Interestingly, group VI TMDCs have different electronic structures depending on their geometrical structure: (i) the trigonal prismatic structure (2H phase) is a semiconductor, and (ii) the octahedral and distorted octahedral (1T and 1T′ phases) are metals.[4−8] 2H-TMDCs have been intensively investigated due to their semiconducting nature; these materials possess various band gaps in the optical range, which are absent in semimetallic graphene.[9−23]

Among group VI TMDCs, 2H-molybdenum ditelluride ($MoTe_2$) has the lowest energy band gap (~1 eV), a low thermal conductivity of ~2 W/(m·K), and a high Seebeck coefficient of 780 $\mu$V/K. These properties might be useful for thermoelectric devices.[24−27] It has been recently reported that the field effect mobility of few-layer 2H-$MoTe_2$ flakes prepared by mechanical exfoliation is comparable to those of 2H-$MoS_2$ and 2H-$MoSe_2$.[28] Since the heavy element of Te in 2H-$MoTe_2$ induces strong spin−orbit coupling, it is useful for valleytronics applications.[29] Alternatively, metallic 1T′-$MoTe_2$ and semiconducting 2H-$MoTe_2$ are promising materials for small-band-gap electronics.[30] Therefore, both 2H-$MoTe_2$ and 1T′-$MoTe_2$ films are in high demand for future uses.

Several synthesis methods, including chemical vapor transport (CVT), electrochemical deposition, physical vapor deposition (PVD), and sonochemical techniques with a post-heat-treatment, have been suggested for the preparation of 2H-$MoTe_2$.[31−34] The CVT synthesis produces high-quality bulk 2H-$MoTe_2$ (limited to millimeter-sized 2H-$MoTe_2$ bulk crystals), but the throughput is low.[31] The electrochemical deposition and PVD methods are rather straightforward for obtaining large-area 2H-$MoTe_2$ films. However, it is still difficult to realize the rational stoichiometry of Mo and Te, without degrading the quality of 2H-$MoTe_2$ films.[32,34] The sonochemical technique has the advantage of producing large-scale 2H-$MoTe_2$ but has

* Address correspondence to kkkim@dongguk.edu, leeyoung@skku.edu.

Received for review April 27, 2015 and accepted June 4, 2015.

**Published online June 04, 2015**
**10.1021/acsnano.5b02511**

difficulties achieving 2H-$MoTe_2$ films with high quality. To our knowledge, the synthesis of large-area and high-quality 2H-$MoTe_2$ and 1T′-$MoTe_2$ films has yet to be successfully accomplished.

Here, we report a facile method to synthesize centimeter-scale 1T′-$MoTe_2$ and 2H-$MoTe_2$ films through tellurization of Mo thin films *via* Te sublimation. Starting with a 1T′-$MoTe_2$ film, phase engineering was realized by tellurization under a Te atmosphere to obtain a 2H-$MoTe_2$ film. To increase the quality of the $MoTe_2$ film, the tellurization rate, sublimation temperature of Te, and tellurization temperature were controlled. The reverse phase transition from 2H to 1T′ is also possible with further tellurization and rapid cooling. The size of the sample was only limited by the chamber size.

## RESULTS AND DISCUSSION

To synthesize $MoTe_2$ films, a two-zone chemical vapor deposition (CVD) system was employed, as illustrated in Figure 1a. To sublimate solid tellurium as a vapor source, the heating zone ($T_1$) was separated from the synthesis zone ($T_2$). A 50 nm thick molybdenum thin film was prepared by a conventional sputter or e-beam evaporator. To control the tellurization rate of the Mo thin film, the temperatures of the tellurium zone ($T_1$) and substrate zone ($T_2$) were separately controlled, as shown in the temperature profile in Figure 1b. For case I (fast tellurization), the Mo substrate ($T_2$) was heated first and followed by ramping up the tellurium zone temperature ($T_2$) (M1). For case II, both zones ($T_1$ and $T_2$) reached 650 °C at the same time (M2). For case III (slow tellurization), the tellurium zone ($T_1$) was heated first, followed by increasing the temperature of the substrate ($T_2$) (M3). Tellurization was carried out for 3 h for all of the samples.

Three different samples were characterized by Raman spectroscopy. In all of the samples, the characteristic Raman-active modes of $E_{1g}$ (117−118 $cm^{-1}$), $E^1_{2g}$ (230−232 $cm^{-1}$), and $A_{1g}$ (171−172 $cm^{-1}$), related to the in-plane modes and out-of plane mode of 2H-$MoTe_2$, were clearly found. This indicates that the 2H-$MoTe_2$ film is successfully synthesized through the tellurization (Figure 1c).[26,35,36] The intensity ratio of $E^1_{2g}$ to $A_{1g}$ for sample M1 is lower than those of M2 and M3, indicating that the 2H-$MoTe_2$ layer is not as well-oriented in M1 compared to the other samples. This will be discussed in detail later. To estimate the quality of the 2H-$MoTe_2$ film, the samples were examined by X-ray diffraction (XRD). The peaks in the XRD pattern, as shown in Figure 1d, were assigned according to the Joint Committee on powder diffraction standards (JCPDS) reference No. 01-072-011. For sample M1, various peaks of the (0002), (0004), (10$\bar{1}$0), (10$\bar{1}$3), (10$\bar{1}$4), (10$\bar{1}$5), and (11$\bar{2}$0) planes in the XRD pattern were observed, indicating that sample M1 is randomly oriented. Alternatively, only the (0002), (0004), (0006), and (0008) planes of 2H-$MoTe_2$ were detected in samples M2 and M3, indicating that these 2H-$MoTe_2$ films are highly oriented in a direction perpendicular to the film plane.

To understand the origin of the highly oriented 2H-$MoTe_2$ films made with the slow tellurization rate, a Mo thin film was annealed under an argon atmosphere without tellurization. While no specific peak in the XRD pattern was observed in the as-deposited Mo film, the (011) and (200) planes of Mo were detected after annealing under an argon atmosphere (see Supporting

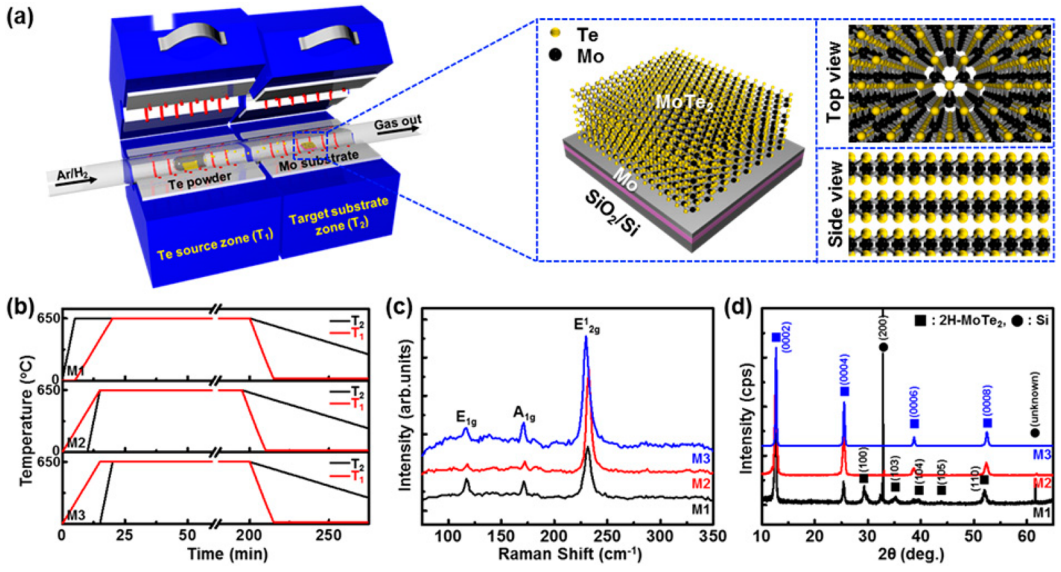


**Figure 1. Synthesis of a large-area 2H-$MoTe_2$ film. (a) Schematic diagram of the synthesis of the 2H-$MoTe_2$ film by two-zone chemical vapor deposition and illustration of the 2H-$MoTe_2$ film on a $SiO_2$/Si substrate. (b) Temperature profile for the Te zone ($T_1$) and Mo substrate zone ($T_2$) for samples M1, M2, and M3. (c,d) Raman spectra and XRD patterns of samples M1, M2, and M3.**

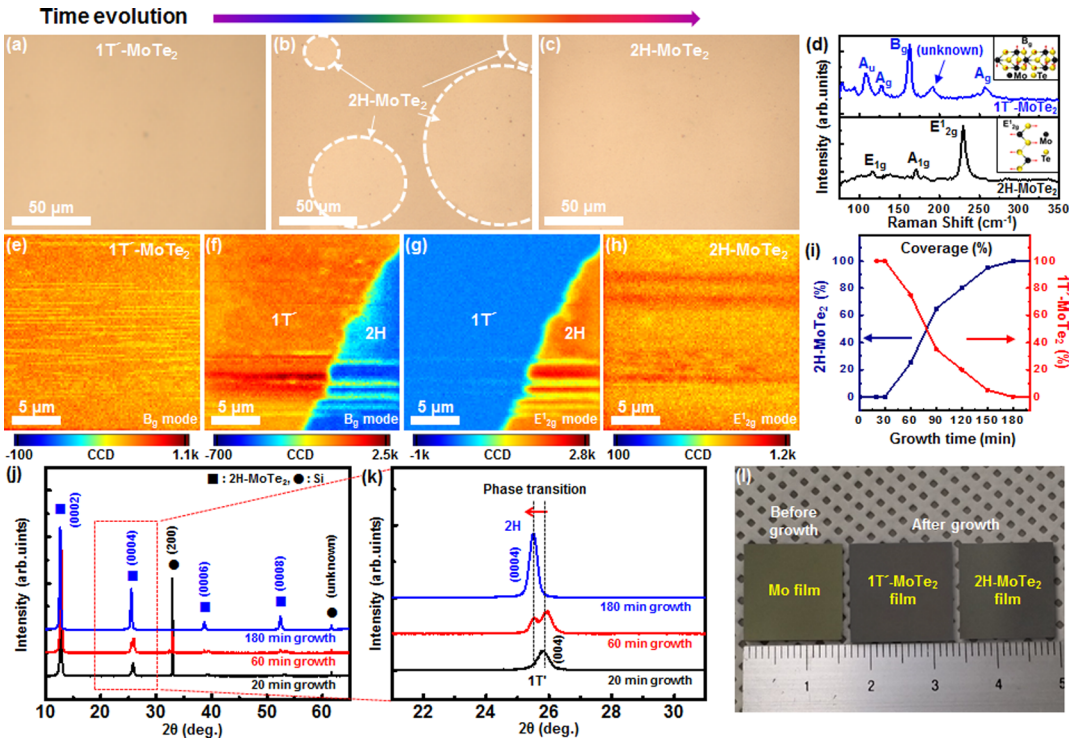


**Figure 2. Time evolution for the growth of 1T′- and 2H-$MoTe_2$ films. (a–c) Optical images of $MoTe_2$ samples after growing for 20, 60, and 180 min, respectively. (d) Representative Raman spectra of (a) (top panel) and (c) (bottom panel). Each Raman spectrum shows 1T′-$MoTe_2$ and 2H-$MoTe_2$, respectively. The insets in both the top and bottom panels illustrate the Raman-active modes of $B_g$ and $E^1_{2g}$. (e–h) Raman mapping images for (e) $B_g$ peak for 20 min of growth, (f,g) $B_g$ and $E^1_{2g}$ peaks for 60 min of growth, respectively, and (h) $E^1_{2g}$ peak for 180 min of growth. (i) Plot of the calculated area of the dark (1T′ phase) and white (2H phase) regions in the optical images as a function of the growth time. (j) XRD patterns of the samples. (k) XRD patterns near the (0004) planes of $MoTe_2$. (l) Photographs of the as-deposited Mo thin film, 1T′-$MoTe_2$ film, and 2H $MoTe_2$ film.**

Information (SI), Figure S1). Therefore, in the case of fast tellurization, the Mo film has already been crystallized prior to tellurization. Tellurization of a crystalline Mo film requires a higher activation energy than that of a noncrystallized Mo film. This may result in a randomly oriented $MoTe_2$ film. Our fast tellurization process is similar to the previous synthesis of $MoS_2$.[37] We emphasize that a noncrystallized Mo film should be maintained through slow tellurization in order to obtain highly oriented 2H-$MoTe_2$ films.

To observe the growth kinetics of 2H-$MoTe_2$ films in more detail, a time evolution experiment was conducted as a function of the tellurization time. Figure 2a–c shows optical images of the samples with different time evolutions of 20, 60, and 180 min, respectively. The slow tellurization scheme was adopted for this experiment (M3). While the color contrast of the 20 min tellurization sample is uniform, circular shapes with a brighter color (indicated by the white dashed line) are scattered from region to region (Figure 2b). At 180 min of tellurization, the contrast becomes uniform again, but bright contrast was shown in Figure 2c. To identify these phases possessing different optical contrasts, the samples were further characterized by Raman spectroscopy. The top and bottom panels in Figure 2d display the representative Raman spectra corresponding to the regions of Figure 2a,c, respectively. Interestingly, while only the characteristic peaks of 1T′-$MoTe_2$, such as $A_u$ (107.0 $cm^{-1}$), $A_g$ (126.9 $cm^{-1}$), $B_g$ (163.0 $cm^{-1}$), and $A_g$ (256.1 $cm^{-1}$), were observed for the region with 20 min of tellurization,[30] the characteristic peaks of 2H-$MoTe_2$ were observed at 180 min of tellurization (without showing peaks related to 1T′-$MoTe_2$). These results imply that the 1T′-$MoTe_2$ film was formed initially, followed by a gradual phase transition to 2H-$MoTe_2$. To track this phase transition, confocal Raman mapping for the $B_g$ phonon mode of 1T′-$MoTe_2$ and for the $E^1_{2g}$ mode of 2H-$MoTe_2$ was conducted, as shown in Figure 2e–h. For 20 min of tellurization, only the 1T′-$MoTe_2$ phase is observed over the whole area (Figure 2e). Figure 2f,g displays the Raman mapping images for the $B_g$ and $E^1_{2g}$ modes at the coexistence region of 1T′-$MoTe_2$ and 2H-$MoTe_2$, respectively, indicating that the 1T′-$MoTe_2$ region is clearly separated from the 2H-$MoTe_2$ region. At the interface between them, the characteristic peaks of both 1T′-$MoTe_2$ and 2H-$MoTe_2$ are observed (see SI, Figure S2). Figure 2h presents the Raman mapping image of only the 2H-$MoTe_2$ phase. Figure 2i shows the time evolution of the areas with brighter color (2H-$MoTe_2$) and darker color (1T′-$MoTe_2$) from the optical images. After 180 min of growth, the Mo thin film was converted completely into 2H-$MoTe_2$.

Figure 2j shows the XRD patterns of the samples for 20, 60, and 180 min of tellurization. The main peaks of

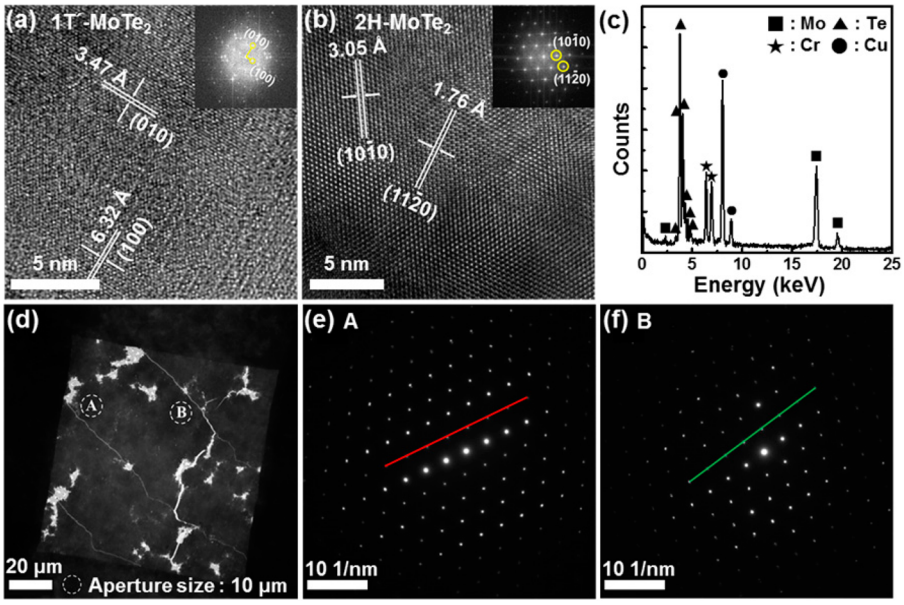


**Figure 3. Structure analysis of 2H-$MoTe_2$ film. TEM images of (a) 1T′-$MoTe_2$ and (b) 2H-$MoTe_2$. The inset of each image shows the corresponding FFT pattern. The *d*-spacings of the (010) and (100) planes for the 1T′ phase are determined to be 3.47 and 6.32 Å, respectively; those of the (10$\bar{1}$0) and (11$\bar{2}$0) planes for the 1H phase are resolved to be 3.05 and 1.76 Å, respectively. (c) EDX spectra of the 2H-$MoTe_2$ film. (d) TEM image of the large-area 2H-$MoTe_2$ film on a TEM grid. (e,f) SAED pattern from the regions of A and B in (d), respectively. The hexagonal spots are rotated by 11.41° from each other.**

the (0002), (0004), (0006), and (0008) planes were detected in all of the samples, although the peak positions were different. Figure 2k shows a narrow range of the XRD pattern near the (0004) plane. Interestingly, while the (0004) peaks of 1T′-$MoTe_2$ and 2H-$MoTe_2$ are split for 60 min of tellurization, only a single peak for 20 and 180 min of tellurization is observed. This result is in good agreement with the results obtained from the Raman analysis. As a consequence, large-area films for both 1T′-$MoTe_2$ and 2H-$MoTe_2$ were obtained, as large as 1.5 × 1.5 $cm^2$, as shown in Figure 2l. The size of the film is limited only by the chamber size. In addition, the thickness of the Mo film was reduced to 8 nm to synthesize the thin $MoTe_2$ film, which was expanded to 20 nm after tellurization (see SI, Figure S3). The 2 nm thick Mo film was not converted to uniform $MoTe_2$ film.

To estimate the quality of the $MoTe_2$ films further, high-resolution transmission electron microscopy (HR-TEM) was used. Figure 3a,b shows HR-TEM images of the 1T′-$MoTe_2$ and 2H-$MoTe_2$ films, respectively. The insets of each image show the fast Fourier transform (FFT) pattern. While the FFT pattern of the 1T′ phase shows a rectangular shape, that of the 2H phase displays a hexagonal shape. Moreover, the *d*-spacings of the (010) and (100) planes for the 1T′ phase are determined to be 3.47 and 6.32 Å, respectively; those of the (10$\bar{1}$0) and (11$\bar{2}$0) planes for the 2H phase are resolved to be 3.05 and 1.76 Å, respectively. These results are well-matched with previous works.[5,30] These distinct results prove the formation of two different phases during growth. In addition, elemental analysis is conducted by using energy-dispersive X-ray spectroscopy (EDX) in TEM (Figure 3c). Mo and Te atoms were detected, and the stoichiometry of the 2H-$MoTe_2$ film is determined to be around 1:2. Evaluating the size of the crystallites of the 2H-$MoTe_2$ film is important for estimating the quality of the samples. In this study, the size of crystallites was measured by using selective area electron diffraction (SAED) equipped in HR-TEM. An aperture diameter of 10 $\mu$m was used for this study. Figure 3d displays the 2H-$MoTe_2$ film on a TEM grid, indicating that the 2H-$MoTe_2$ film is highly continuous. Figure 3e,f presents the SAED patterns corresponding to the regions of A and B in Figure 3d, respectively. Each SAED pattern shows definite hexagonal dots, indicating that the 2H-$MoTe_2$ film is single-crystalline and that the size of the crystallite is at least 10 $\mu$m in diameter. In addition, the 2H-$MoTe_2$ layers are stacked and highly ordered. The two hexagonal dots for regions A and B are rotated by 11.4° from each other, indicating that the 2H-$MoTe_2$ films are polycrystalline (see SI, Figure S4).

To further understand the growth behavior of $MoTe_2$ films, the cross-sectional TEM technique was employed, as shown in Figure 4a–l. For 20 min of growth (Figure 4a–d), three distinct regions are observed: (b) a 1T′ phase near the top of the sample, (c) noncrystallized Mo in the middle region, and (d) an unidentified $Mo_xTe_y$ region near the interface with $SiO_2$. This implies that the 1T′-$MoTe_2$ phase is initiated from the top of the Mo film. The presence of the 1T′ phase was confirmed by measuring the interlayer distance (0.691 nm), which is well-matched with the XRD data. Interestingly, the presence of Te was found in the bottom region, as confirmed by EDX mapping (see SI, Figure S5). This might be attributed to the diffusion of Te between $SiO_2$ and the Mo film. For 60 min of growth, three distinct regions were

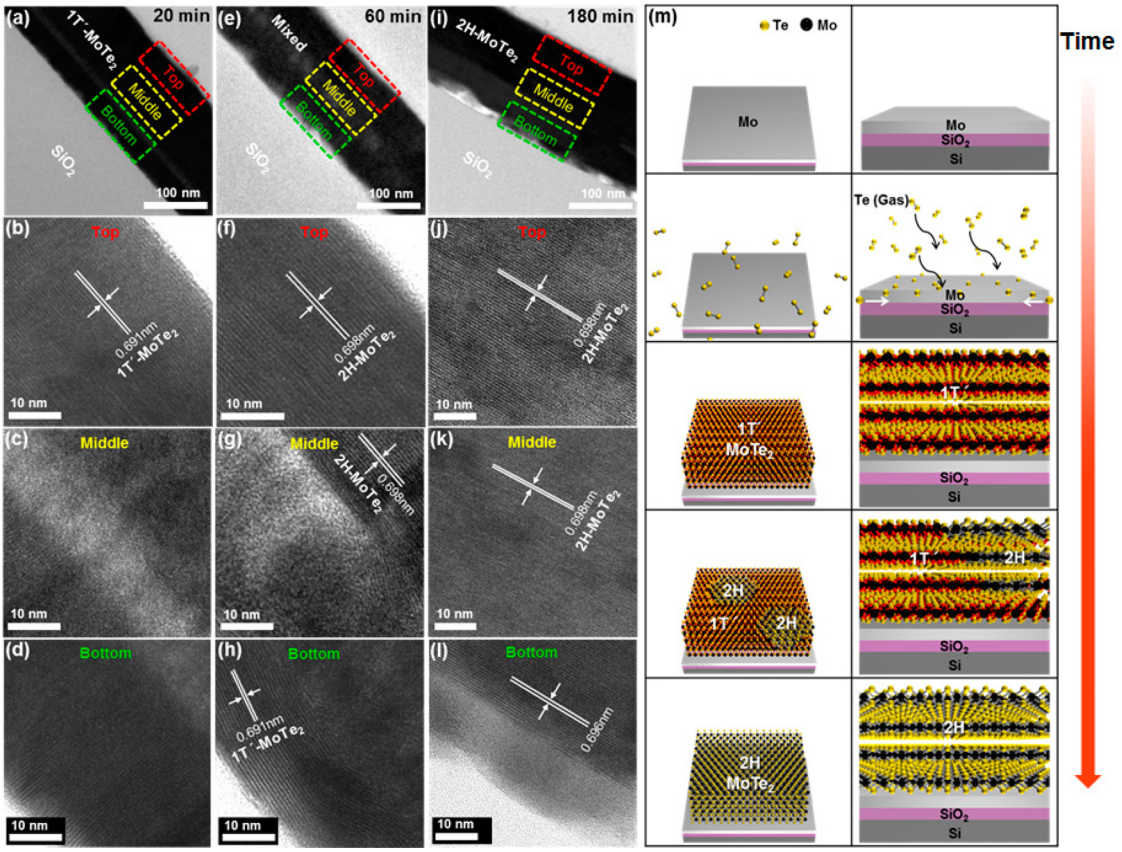


**Figure 4. Cross-sectional TEM images of 1T′- and 2H-$MoTe_2$ films. Cross-sectional TEM images of the samples corresponding to (a–d) 20 min, (e–h) 60 min, and (i–l) 180 min of growth. Three different regions, corresponding to the top, middle, and bottom regions in (a), (e), and (i), are analyzed in order to understand the phase transition. The two phases (1T′ and 2H) are differentiated by measuring the different interlayer distances, which are 0.691 and 0.698 nm, respectively. (m) Schematic of the phase-engineered growth of the 2H-$MoTe_2$ film.**

also observed, but the 2H phase (instead of the 1T′ phase) is observed in the top region. This is again identified by measuring the interlayer distance, which was found to be 0.698 nm (as opposed to 0.691 nm). This result is also in good agreement with the results from the XRD measurements (Figure 4f,g). In the bottom region (Figure 4h), the 1T′ phase was observed. In addition, some regions in the top region still showed the 1T′-$MoTe_2$ phase instead of the 2H-$MoTe_2$ phase, which is congruent with the optical image of Figure 2b (see SI, Figure S6). For 180 min of growth, most regions are converted to the 2H phase, except for areas near the bottom region (Figure 4j–l). The interlayer distance in the bottom region is ~0.696 nm, which is a value in between those of the 2H and 1T′ phases. This implies that the bottom region is still under a transition process. We carefully confirmed that the growth results observed for all of the regions were typical, indicating that growth occurs uniformly (see SI, Figure S7). Figure 4m illustrates a schematic diagram for the sequence of growth behavior based on our analysis. In the initial stage, Te diffuses into the Mo bulk through the top of the Mo film and through the bottom between the Mo and $SiO_2$ films to form 1T′-$MoTe_2$. After a prolonged period of time, the 1T′-$MoTe_2$ layers are converted into 2H-$MoTe_2$.

It has been predicted theoretically that the cohesive energy difference between 1T′-$MoTe_2$ and 2H-$MoTe_2$, revealed by calculation, is <0.1 eV at 0 K.[38,39] The thermal vibration energy can promote the phase transition with mechanical strain: the 2H phase is stable under zero strain, and the 1T′ phase is stable under tensile strain. In our case, 1T′-$MoTe_2$ was first synthesized and a phase transition occurred with prolonged tellurization time. Therefore, the phase transition in this study might be attributed to the relaxation of the tensile strain due to the presence of excess of Te.

Furthermore, we were able to realize the reverse phase transition by reducing the partial pressure of Te. This was done by using a lower temperature for $T_1$ (460 °C instead of 650 °C) with the same temperature for $T_2$ (see SI, experimental method S1 and Figure S8). When the 2H-$MoTe_2$ film was further annealed at low Te vapor pressure (low temperature, $T_1$), the reverse phase transition from 2H-$MoTe_2$ into 1T′-$MoTe_2$ took place. However, upon annealing in the absence of excess Te, a $Mo_6Te_8$ film was obtained due to the evaporation of Te in 2H-$MoTe_2$ (see SI, Figure S9). These results imply that controlling the Te content in $MoTe_2$ films is a key factor for engineering the phase transition.

## CONCLUSION

In summary, we have successfully synthesized centimeter-scale 1T′ and 2H-$MoTe_2$ films *via* reversible phase transition engineering. The phase transition is driven by the mechanical strain and relaxation caused by the variable Te content. To obtain highly oriented 2H-$MoTe_2$ films, slow tellurization is essential. This work paves the way for the synthesis of a variety of large-area and high-quality multilayer TMDCs and promotes the study of phase transitions in TMDCs.

## EXPERIMENTAL SECTION

**Synthesis of 1T′ and 2H-$MoTe_2$ Films.** The noncrystallized 50 nm thick Mo thin film was deposited on a 300 nm thick $SiO_2$/Si substrate with an e-beam evaporator or sputter. To grow the $MoTe_2$ film, 2 g of Te powder (Sigma-Aldrich) and the Mo thin film were mounted in a two-zone CVD (Figure 1a). To control the tellurization rate, the temperatures of the Te zone ($T_1$) and Mo film zone ($T_2$) were controlled separately. During the growth process, argon and hydrogen were flowed at rates of 500 and 100 sccm, respectively. For fast tellurization, $T_2$ was first heated to 650 °C and then $T_1$ was ramped up to 650 °C at a ramping rate of 30 °C/min. For the slow tellurization rate, $T_1$ was first heated to 650 °C and then $T_2$ was heated to 650 °C once $T_1$ reached 650 °C. The detailed temperature profile is shown in Figure 1b. When the temperature reached 650 °C, growth was carried out for 3 h. For 1T′-MoTe, growth was conducted for 20 min with the slow tellurization rate. After growth, $T_1$ was cooled rapidly by opening the chamber; $T_2$ was then cooled to room temperature at a rate of −5 °C/min.

**Characterization.** To characterize the optical and physical structures of the $MoTe_2$ films, optical microscopy (Axio Imager 2, CARL ZEISS), Raman spectroscopy (XperRam 200, Nano Base) with an excitation energy of 2.33 eV, XRD (SmartLab, Rigaku), AFM (SPA 400, SEIKO), and TEM (JEM ARM 200F, JEOL Ltd.) were used. For the TEM measurements, the samples were transferred using the conventional poly(methyl methacrylate) (PMMA) method.[40,41] To detach the $MoTe_2$ film from the $SiO_2$/Si substrate, the PMMA-coated $MoTe_2$ film was immersed in a buffered oxide etchant (1178−03, J.T. Baker) for 15 min. The PMMA/$MoTe_2$ film was washed with distilled water several times. The resulting film was transferred onto a TEM grid. The PMMA layer was removed by the application of acetone and annealing at 350 °C for 5 h. To obtain cross-sectional TEM images, the samples were prepared with a focused ion beam (JIB-4601F, JEOL Ltd.). To analyze the chemical elements, EDX in a TEM was employed.

*Conflict of Interest:* The authors declare no competing financial interest.

*Supporting Information Available:* Experimental method S1 and Figures S1−S9. The Supporting Information is available free of charge on the ACS Publications website at DOI: 10.1021/acsnano.5b02511.

*Acknowledgment.* This work was supported by IBS-R011-D1 and in part by BK21-Plus through Ministry of Education, Korea. S.M.K. acknowledge support from the KIST Institutional Program. We would like to thank Prof. Heejun Yang and Suyeon Cho for their discussion about the 1T′-$MoTe_2$ phase.

## REFERENCES AND NOTES

1. Bertolazzi, S.; Brivio, J.; Kis, A. Stretching and Breaking of Ultrathin $MoS_2$. *ACS Nano* **2011**, *5*, 9703–9709.
2. Chhowalla, M.; Shin, H. S.; Eda, G.; Li, L. J.; Loh, K. P.; Zhang, H. The Chemistry of Two-Dimensional Layered Transition Metal Dichalcogenide Nanosheets. *Nat. Chem.* **2013**, *5*, 263–275.
3. Shim, G. W.; Yoo, K.; Seo, S. B.; Shin, J.; Jung, D. Y.; Kang, I. S.; Ahn, C. W.; Cho, B. J.; Choi, S. Y. Large-Area Single-Layer $MoSe_2$ and Its van der Waals Heterostructures. *ACS Nano* **2014**, *8*, 6655–6662.
4. Wilson, J. A.; Yoffe, A. D. The Transition Metal Dichalcogenides Discussion and Interpretation of the Observed Optical, Electrical and Structural Properties. *Adv. Phys.* **1969**, *18*, 193–335.
5. Dawson, W.; Bullett, D. Electronic Structure and Crystallography of $MoTe_2$ and $WTe_2$. *J. Phys. C: Solid State Phys.* **1987**, *20*, 6159–6174.
6. Enyashin, A. N.; Yadgarov, L.; Houben, L.; Popov, I.; Weidenbach, M.; Tenne, R.; Bar-Sadan, M.; Seifert, G. New Route for Stabilization of 1T-$WS_2$ and $MoS_2$ Phases. *J. Phys. Chem. C* **2011**, *115*, 24586–24591.
7. Eda, G.; Fujita, T.; Yamaguchi, H.; Voiry, D.; Chen, M. W.; Chhowalla, M. Coherent Atomic and Electronic Heterostructures of Single-Layer $MoS_2$. *ACS Nano* **2012**, *6*, 7311–7317.
8. Vellinga, M.; De Jonge, R.; Haas, C. Semiconductor to Metal Transition in $MoTe_2$. *J. Solid State Chem.* **1970**, *2*, 299–302.
9. Balakrishnan, K.; Ramasamy, P. Study of Anomalous Electrical Behaviour of Molybdenum Ditelluride Single Crystals. *J. Cryst. Growth* **1994**, *137*, 309–311.
10. Podzorov, V.; Gershenson, M. E.; Kloc, C.; Zeis, R.; Bucher, E. High-Mobility Field-Effect Transistors Based on Transition Metal Dichalcogenides. *Appl. Phys. Lett.* **2004**, *84*, 3301–3303.
11. Hinnemann, B.; Moses, P. G.; Bonde, J.; Jorgensen, K. P.; Nielsen, J. H.; Horch, S.; Chorkendorff, I.; Norskov, J. K. Biomimetic Hydrogen Evolution: $MoS_2$ Nanoparticles as Catalyst for Hydrogen Evolution. *J. Am. Chem. Soc.* **2005**, *127*, 5308–5309.
12. Jaramillo, T. F.; Jorgensen, K. P.; Bonde, J.; Nielsen, J. H.; Horch, S.; Chorkendorff, I. Identification of Active Edge Sites for Electrochemical $H_2$ Evolution from $MoS_2$ Nanocatalysts. *Science* **2007**, *317*, 100–102.
13. Bonde, J.; Moses, P. G.; Jaramillo, T. F.; Norskov, J. K.; Chorkendorff, I. Hydrogen Evolution on Nano-particulate Transition Metal Sulfides. *Faraday Discuss.* **2008**, *140*, 219–231.
14. Mak, K. F.; He, K. L.; Shan, J.; Heinz, T. F. Control of Valley Polarization in Monolayer $MoS_2$ by Optical Helicity. *Nat. Nanotechnol.* **2012**, *7*, 494–498.
15. Zeng, H. L.; Dai, J. F.; Yao, W.; Xiao, D.; Cui, X. D. Valley Polarization in $MoS_2$ Monolayers by Optical Pumping. *Nat. Nanotechnol.* **2012**, *7*, 490–493.
16. Karunadasa, H. I.; Montalvo, E.; Sun, Y. J.; Majda, M.; Long, J. R.; Chang, C. J. A Molecular $MoS_2$ Edge Site Mimic for Catalytic Hydrogen Generation. *Science* **2012**, *335*, 698–702.
17. Geim, A. K.; Grigorieva, I. V. van der Waals heterostructures. *Nature* **2013**, *499*, 419–425.
18. Voiry, D.; Yamaguchi, H.; Li, J. W.; Silva, R.; Alves, D. C. B.; Fujita, T.; Chen, M. W.; Asefa, T.; Shenoy, V. B.; Eda, G.; et al. Enhanced Catalytic Activity in Strained Chemically Exfoliated $WS_2$ Nanosheets for Hydrogen Evolution. *Nat. Mater.* **2013**, *12*, 850–855.
19. Voiry, D.; Salehi, M.; Silva, R.; Fujita, T.; Chen, M. W.; Asefa, T.; Shenoy, V. B.; Eda, G.; Chhowalla, M. Conducting $MoS_2$ Nanosheets as Catalysts for Hydrogen Evolution Reaction. *Nano Lett.* **2013**, *13*, 6222–6227.
20. Jariwala, D.; Sangwan, V. K.; Lauhon, L. J.; Marks, T. J.; Hersam, M. C. Emerging Device Applications for Semiconducting Two-Dimensional Transition Metal Dichalcogenides. *ACS Nano* **2014**, *8*, 1102–1120.
21. Lopez-Sanchez, O.; Lembke, D.; Kayci, M.; Radenovic, A.; Kis, A. Ultrasensitive Photodetectors Based on Monolayer $MoS_2$. *Nat. Nanotechnol.* **2013**, *8*, 497–501.
22. Choi, W.; Cho, M. Y.; Konar, A.; Lee, J. H.; Cha, G. B.; Hong, S. C.; Kim, S.; Kim, J.; Jena, D.; Joo, J.; Kim, S. High-Detectivity Multilayer $MoS_2$ Phototransistors with Spectral Response

from Ultraviolet to Infrared. *Adv. Mater.* **2012**, *24*, 5832–5836.
23. Wang, Q. H.; Kalantar-Zadeh, K.; Kis, A.; Coleman, J. N.; Strano, M. S. Electronics and Optoelectronics of Two-Dimensional Transition Metal Dichalcogenides. *Nat. Nanotechnol.* **2012**, *7*, 699–712.
24. Ma, Y. D.; Dai, Y.; Guo, M.; Niu, C. W.; Lu, J. B.; Huang, B. B. Electronic and Magnetic Properties of Perfect, Vacancy-Doped, and Nonmetal Adsorbed $MoSe_2$, $MoTe_2$ and $WS_2$ Monolayers. *Phys. Chem. Chem. Phys.* **2011**, *13*, 15546–15553.
25. Kumar, A.; Ahluwalia, P. Electronic Structure of Transition Metal Dichalcogenides Monolayers 1H-$MX_2$ (M = Mo, W; X = S, Se, Te) from Ab-Initio Theory: New Direct Band Gap Semiconductors. *Eur. Phys. J. B* **2012**, *85*, 1–7.
26. Balendhran, S.; Walia, S.; Nili, H.; Ou, J. Z.; Zhuiykov, S.; Kaner, R. B.; Sriram, S.; Bhaskaran, M.; Kalantar-zadeh, K. Two-Dimensional Molybdenum Trioxide and Dichalcogenides. *Adv. Funct. Mater.* **2013**, *23*, 3952–3970.
27. Brixner, L. Preparation and Properties of the Single Crystalline AB 2-Type Selenides and Tellurides of Niobium, Tantalum, Molybdenum and Tungsten. *J. Inorg. Nucl. Chem.* **1962**, *24*, 257–263.
28. Pradhan, N. R.; Rhodes, D.; Feng, S. M.; Xin, Y.; Memaran, S.; Moon, B. H.; Terrones, H.; Terrones, M.; Balicas, L. Field-Effect Transistors Based on Few-Layered $\alpha$-$MoTe_2$. *ACS Nano* **2014**, *8*, 5911–5920.
29. Xiao, D.; Liu, G.-B.; Feng, W.; Xu, X.; Yao, W. Coupled Spin and Valley Physics in Monolayers of $MoS_2$ and Other Group-VI Dichalcogenides. *Phys. Rev. Lett.* **2012**, *108*, 196802.
30. Keum, D. H.; Cho, S.; Kim, J. H.; Choe, D. H.; Sung, H. J.; Kan, M.; Kang, H.; Hwang, J. Y.; Kim, S. W.; Yang, H.; et al. Bandgap Opening in Few-Layered Monoclinic $MoTe_2$. *Nat. Phys.* **2015**, *11*, 482–486.
31. Al-Hilli, A.; Evans, B. The Preparation and Properties of Transition Metal Dichalcogenide Single Crystals. *J. Cryst. Growth* **1972**, *15*, 93–101.
32. Mei Ying, L.; Mazlan, N. H.; Joseph, T. Synthesis and Characterization of $MoTe_2$ Thin Films for Photoelectrochemical Cell Applications. *Proceedings of United Kingdom—Malaysia—Ireland Engineering Science Conference 2011*; Kuala Lumpur, Malaysia, July 12—14, **2011**.
33. Qiu, L. H.; Pol, V. G.; Wei, Y.; Gedanken, A. A Two-Step Process for the Synthesis of $MoTe_2$ Nanotubes: Combining a Sonochemical Technique with Heat Treatment. *J. Mater. Chem.* **2003**, *13*, 2985–2988.
34. Srivastava, S. K.; Guettari, N.; Bernede, J. C. Growth of Textured Nonstoichiometric $MoTe_2$ Films from Mo/Te Layers and Their Use as Precursor in The Synthesis of $MoTe_{2-x}S_x$ Films. *Solid State Commun.* **2004**, *132*, 601–606.
35. Sugai, S.; Ueda, T. High-Pressure Raman Spectroscopy in the Layered Materials 2H-$MoS_2$, 2H-$MoSe_2$, and 2H-$MoTe_2$. *Phys. Rev. B* **1982**, *26*, 6554.
36. Yamamoto, M.; Wang, S. T.; Ni, M. Y.; Lin, Y. F.; Li, S. L.; Aikawa, S.; Jian, W. B.; Ueno, K.; Wakabayashi, K.; Tsukagoshi, K. Strong Enhancement of Raman Scattering from a Bulk-Inactive Vibrational Mode in Few-Layer $MoTe_2$. *ACS Nano* **2014**, *8*, 3895–3903.
37. Kong, D. S.; Wang, H. T.; Cha, J. J.; Pasta, M.; Koski, K. J.; Yao, J.; Cui, Y. Synthesis of $MoS_2$ and $MoSe_2$ Films with Vertically Aligned Layers. *Nano Lett.* **2013**, *13*, 1341–1347.
38. Duerloo, K. A. N.; Li, Y.; Reed, E. J. Structural Phase Transitions in Two-Dimensional Mo- and W-Dichalcogenide Monolayers. *Nat. Commun.* **2014**, *5*, 4214.
39. ASM Alloy Phase Diagrams Database Home Page. http://www1.asminternational.org/asmenterprise/APD/ViewAPD.aspx?id=901666 (accessed April 10, 2015).
40. Kim, K. S.; Zhao, Y.; Jang, H.; Lee, S. Y.; Kim, J. M.; Kim, K. S.; Ahn, J. H.; Kim, P.; Choi, J. Y.; Hong, B. H. Large-Scale Pattern Growth of Graphene Films for Stretchable Transparent Electrodes. *Nature* **2009**, *457*, 706–710.
41. Reina, A.; Jia, X. T.; Ho, J.; Nezich, D.; Son, H. B.; Bulovic, V.; Dresselhaus, M. S.; Kong, J. Large Area, Few-Layer Graphene Films on Arbitrary Substrates by Chemical Vapor Deposition. *Nano Lett.* **2009**, *9*, 30–35.